Efficient chip-based optical parametric oscillators from 590 nm to 1150 nm

Jordan R. Stone,[1,2] Xiyuan Lu,[1,2] Gregory Moille,[1,2] and Kartik Srinivasan[1,2]
[1)] *Joint Quantum Institute, NIST/University of Maryland, College Park, MD 20742 USA*
[2)] *National Institute for Standards and Technology, Gaithersburg, MD 20899 USA*

(*Electronic mail: jstone12@umd.edu)

(Dated: 5 December 2022)

Optical parametric oscillators are widely used to generate coherent light at frequencies not accessible by conventional laser gain. However, chip-based parametric oscillators operating in the visible spectrum have suffered from pump-to-signal conversion efficiencies typically less than 0.1 %. Here, we demonstrate efficient optical parametric oscillators based on silicon nitride photonics that address frequencies between 260 THz (1150 nm) and 510 THz (590 nm). Pumping silicon nitride microrings near 385 THz (780 nm) yields monochromatic signal and idler waves with unprecedented output powers in this wavelength range. We estimate on-chip output powers (separately for the signal and idler) between 1 mW and 5 mW and conversion efficiencies reaching ≈ 15 %. Underlying this improved performance is our development of pulley waveguides for broadband near-critical coupling, which exploits a fundamental connection between the waveguide-resonator coupling rate and conversion efficiency. Finally, we find that mode competition reduces conversion efficiency at high pump powers, thereby constraining the maximum realizable output power. Our work proves that optical parametric oscillators built with integrated photonics can produce useful amounts of visible laser light with high efficiency.

I. INTRODUCTION

Lasers operating at visible and near-infrared (NIR) wavelengths are essential to modern science and technology[1–4], but affordable systems typically suffer from poor spectral purity and gaps in spectral coverage, while higher-performance options are large and expensive. The latter often rely on bulk nonlinear optics to spectrally translate longer-wavelength lasers to the targeted frequency, employing either sum-frequency or second-harmonic generation in $\chi^{(2)}$-nonlinear media[5–7]. Their operational complexity and substantial power consumption (they often require liquid cooling systems) renders them impractical in many situations. Hence, it is desirable to transition the nonlinear wavelength conversion to a more scalable nonlinear optics platform, e.g., integrated photonics.

One approach is to leverage the wavelength flexibility inherent to optical parametric oscillators using nonlinear microresonators, which possess large optical quality factors (Q) and small mode volumes to intensify circulating light and promote efficient nonlinear interactions[8,9]. Recent studies of microresonator-based optical parametric oscillators (μOPOs) have demonstrated broad spectral separation between pump and generated light[10–12], low-power operation[13,14], and visible-wavelength access[15]. In particular, operating in the visible spectrum presents specific challenges: Stronger material dispersion, larger scattering losses that reduce quality factors, and shorter evanescent field decay lengths that impede waveguide coupling. While both $\chi^{(2)}$ and $\chi^{(3)}$ μOPOs offer some wavelength flexibility, $\chi^{(3)}$ systems are useful to generate visible light from a NIR pump; moreover, their natural availability in the popular silicon photonics platform[16] can enable their scalable fabrication and integration with other components, including pump lasers[17]. On the other hand, the reported or inferred (e.g., from optical spectra) conversion efficiencies are $\lesssim 0.1\%$[10,13,15,18–20], and the available output power is far too low for many applications (e.g., <10 μW for previous visible μOPOs[15]). Realizing higher conversion efficiencies and output powers would enable a wide range of on-chip applications and broaden the reach of silicon photonics in the visible spectrum.

Here, we demonstrate efficient μOPOs that generate coherent light within the spectral window between 260 THz and 510 THz (590 nm and 1150 nm). We measure conversion efficiencies between 3.5 % and 14.5 % with corresponding on-chip output powers greater than 1 mW (and as high as 5 mW). Our results spring from efficient broadband waveguide-resonator coupling, which we realize with pulley-waveguide geometries designed using coupled-mode simulations. Notably, previous μOPO works have implemented such geometries to minimize threshold power[13]; in contrast, our goal is to maximize output power using pulleys that operate in a fundamentally different regime. In the rest of this paper, we first introduce the key μOPO physics and specify our experimental procedures. Then, we explain our coupled-mode simulations and present measurements to confirm their accuracy. Next, we present the optical spectra of 16 different μOPOs, from which we determine output powers and conversion efficiencies. Finally, we show how parasitic nonlinear processes currently constrain the maximum realizable output power. Our work is an important step forward in the quest for practical, chip-based sources of visible laser light using nonlinear optics.

The μOPOs we consider generate monochromatic signal and idler waves from a continuous-wave (CW) pump laser through resonantly-enhanced degenerate four wave mixing (FWM), as depicted in Fig. 1a[21]. In experiments, we pump a fundamental transverse-electric (TE0) eigenmode of a silicon nitride microring near 385 THz, and FWM transfers energy to TE0 signal and idler modes. In principle, the range of accessible output frequencies, as constrained only by energy

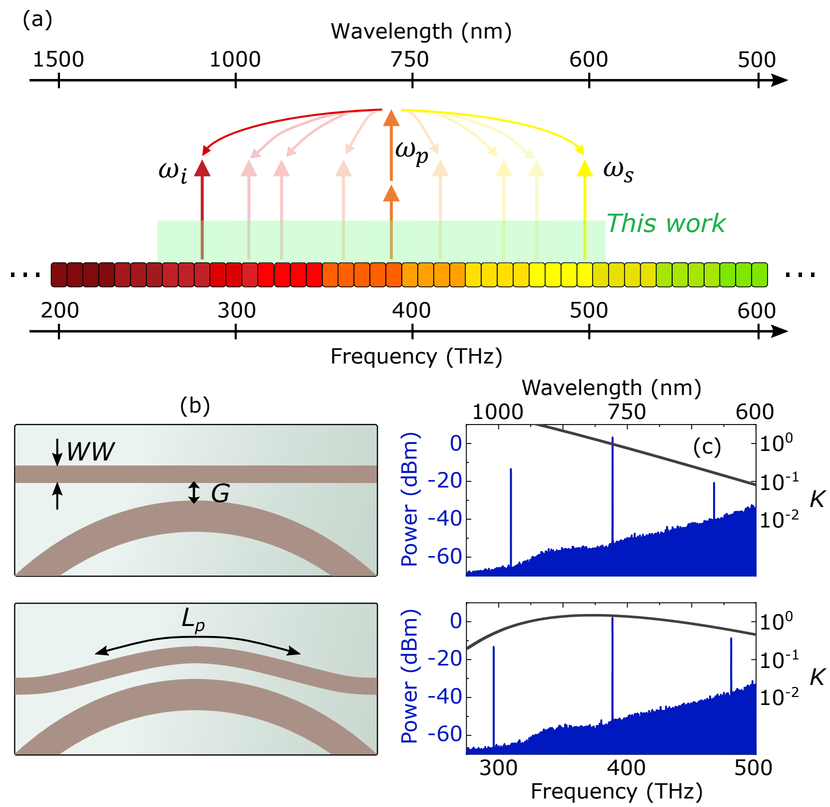

FIG. 1. **Achieving high conversion efficiency (*CE*) across a wide spectral band with microresonator-based optical parametric oscillators (μOPOs).** (a) Conceptual depiction of $\chi^{(3)}$ optical parametric oscillation. Two pump photons (frequency ω_p) are converted to one signal (ω_s) photon and one idler (ω_i) photon. We focus on generating different μOPOs (faded arrows) within the spectral window between 260 THz and 510 THz, as marked by the green stripe. (b) Depictions of microring couplers, as viewed from above, which rely on evanescent coupling between the microring and either a straight access waveguide (top panel) or a pulley waveguide (bottom panel). Couplers are defined by three geometric parameters: the waveguide width, WW, the gap (or distance) between the microring and waveguide, G, and the length of waveguide, L_p, that runs parallel to the microring. (c) Simulated coupling ratios, K (gray), and measured μOPO spectra (blue) for identical microrings with different coupling geometries. The top panel data corresponds to a straight waveguide ($WW = 375$ nm; $G = 125$ nm) coupler, while bottom panel data corresponds to a pulley waveguide (same WW and G; $L_\mathrm{p} = 3\ \mu$m).

conservation, is DC to $2\omega_\mathrm{p}$, where ω_p is the pump frequency. However, in practice this range is dictated by the group velocity dispersion (GVD), which must be engineered such that FWM to the targeted signal and idler modes is favored (simultaneously phase- and frequency-matched), but FWM to other modes is suppressed. In the Supplemental Material, we recount our approach to dispersion engineering that is also described in Ref. 15.

A separate challenge is to ensure that pump power is efficiently converted into output signal or idler power. Hence, we define the on-chip conversion efficiency as:

$$CE = \frac{P_\mathrm{s(i)}}{P_\mathrm{in}}, \tag{1}$$

where $P_\mathrm{s(i)}$ is the signal (idler) power in the waveguide output, and P_in is the pump power in the waveguide input. Recent theoretical work has derived the maximum obtainable CE as:

$$CE^\mathrm{max}_\mathrm{s(i)} = \frac{1}{2}\frac{\kappa_\mathrm{s(i)}\kappa_\mathrm{p}}{\Gamma_{s(i)}\Gamma_\mathrm{p}}\frac{\omega_\mathrm{s(i)}}{\omega_\mathrm{p}}, \tag{2}$$

where $\kappa_\mathrm{s(i)}$ and κ_p are the waveguide-resonator coupling rates of the signal (idler) and pump modes, $\Gamma_\mathrm{s(i)}$ and Γ_p are the total loss rates (i.e., loaded linewidths) of the signal (idler) and pump modes, and $\omega_\mathrm{s(i)}$ and ω_p are the frequencies of the signal (idler) and pump light, respectively[10]. Clearly, obtaining large CE involves engineering κ for both the pump mode and targeted signal/idler modes. Such coupling engineering is a common problem in the nonlinear optics of Kerr microresonators; it arises, for example, in the efficient extraction of octave-spanning Kerr microcombs[22]. The problem is that, given a straight waveguide evanescently coupled to a microring resonator, κ decreases exponentially with frequency due to decreasing overlap of the microring mode with the waveguide mode. Hence, when the pump mode is critically coupled, the signal mode is undercoupled, resulting in low CE. Moreover, when ω_s is a visible frequency, the smaller evanescent decay length compared to NIR frequencies exacerbates the challenge. One solution is to utilize so-called pulley waveguides, which increase the physical distance over which the waveguide and microring can exchange energy[22–24]. Figure 1b illustrates the physical differences between straight-waveguide couplers (top panel) and pulley-waveguide couplers (bottom panel), and it depicts the three geometric parameters that define such couplers in our study: The waveguide width, WW, the waveguide-resonator gap, G, and the pulley length, L_p (which approaches zero in the straight-waveguide limit). In Fig. 1c, we present measurements of μOPO spectra extracted from nominally identical microrings using either a straight-waveguide coupler (top panel) or a pulley-waveguide coupler (bottom panel). These measurements are representative of other comparisons between the two coupling schemes. While P_i is roughly the same in each case, P_s is approximately 20× greater in the pulley waveguide. To explain the result, we show in the same panels the simulated coupling ratio, defined as $K = \kappa/\gamma$ (equivalently, $K = Q_\mathrm{i}/Q_\mathrm{c}$, where Q_i and Q_c are the intrinsic and coupling quality factors, respectively), where $\gamma = \Gamma - \kappa$ is the intrinsic loss rate. Near ω_s, K is $\approx 8\times$ higher for the pulley-waveguide coupler.

II. DESIGN AND TEST OF WAVEGUIDE COUPLERS

To design couplers for testing, we simulate κ spectra for a variety of coupling geometries with the goal of achieving $K \approx 1$ (i.e., critical coupling) at frequencies between 260 THz and 510 THz. Notably, achieving high CE only requires that κ be optimized at ω_p and either ω_s or ω_i, depending on which output wave (signal or idler) is to be used. (Moreover, ideally, the unused wave is undercoupled to reduce threshold power). At the same time, broadband near-critical coupling is preferable, since then a single coupling geometry is robust against design imperfections, and it may be used for many different μOPOs. Our simulations are based on a coupled mode theory for optical waveguides[25], which calculates κ according to:

$$\kappa = \frac{c}{2\pi R n_\mathrm{g}} |k_\mathrm{t}|^2, \tag{3}$$

where R is the microring outer radius, c is the speed of light, n_g is the group refractive index, and k_t is a coupling coefficient defined as:

$$k_\mathrm{t} = \frac{i\omega}{4} \int_L \left[\int_A (\varepsilon_\mathrm{WG} - \varepsilon_\mathrm{R}) \boldsymbol{E}_\mathrm{R}^* \cdot \boldsymbol{E}_\mathrm{WG} \mathrm{d}r\mathrm{d}z \right] e^{i\phi} \mathrm{d}l, \tag{4}$$

where $\varepsilon_{\mathrm{WG(R)}}$ is the dielectric permittivity of the access waveguide (microring), $\boldsymbol{E}_{\mathrm{WG(R)}}$ is the electric field of the waveguide (microring) eigenmode, and ϕ is an accumulated phase accounting for the difference in the waveguide and microring propagation constants. The coordinates r and z are horizontal and vertical coordinates in-plane with the microring/waveguide cross section, as labeled in the Fig. 2a inset, and l follows the direction of light propagation. The central integral in Eq. (4) evaluates the evanescent overlap between the microring and waveguide modes at the frequency

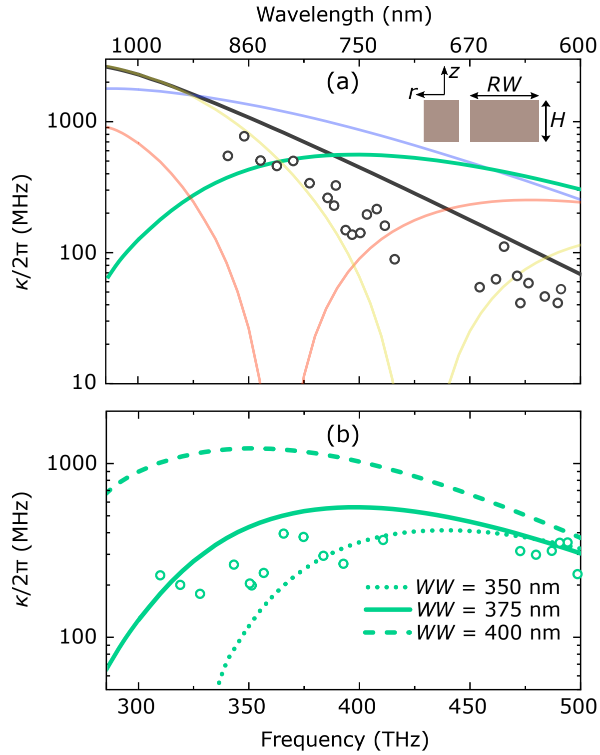

FIG. 2. **Design, simulation, and measurement of coupling rate (κ).** (a) Simulated κ spectra for a silicon nitride (SiN) microring with waveguide parameters $WW = 375$ nm, $G = 150$ nm, and $L_\mathrm{p} = 0$ μm (bold gray curve), 2 μm (faded blue), 3 μm (green), 4 μm (faded red), and 5 μm (faded yellow). The circular data points indicate measured κ values for the coupler with $L_\mathrm{p} = 0$ μm. The inset depicts the waveguide/microring cross section, including labels for the ring width (RW) and height (H), and shows axes for the coordinates r and z over which we integrate Eq. 4. (b) Simulated κ spectra for a SiN microring with waveguide parameters $G = 150$ nm, $L_\mathrm{p} = 3$ μm, and different values of WW. The circular data points indicate measured κ values for the coupler with $WW = 375$ nm. The uncertainty in the measured κ values as determined from a nonlinear least squares fit to the resonator transmission spectrum is smaller than the data point size.

ω. For more details, see Ref.[22]. Figure 2a shows simulated κ spectra for a SiN microring with $R = 25$ μm, ring width $RW = 825$ nm, and height $H = 500$ nm, which are chosen to suitably engineer the GVD (see Supplemental Material). In addition, we choose $WW = 375$ nm, $G = 150$ nm, and L_p from 0 μm (i.e., a straight-waveguide coupler) to 5 μm. Increasing L_p results in larger κ at higher frequencies compared to the straight-waveguide coupler (dark grey line), but it introduces resonances in the κ spectra (i.e., regions where $\kappa \to 0$) that arise from the coherent energy exchange between the microring and waveguide. These resonances blueshift when L_p is increased. Based on these data, we select $L_\mathrm{p} = 3$ μm for further study because it minimizes variations in κ over the targeted spectral region.

Next, we optimize WW and G. The predominant effect of changing G is to vertically shift the entire κ spectrum; i.e., G has little impact on the spectral location of the coupling reso-

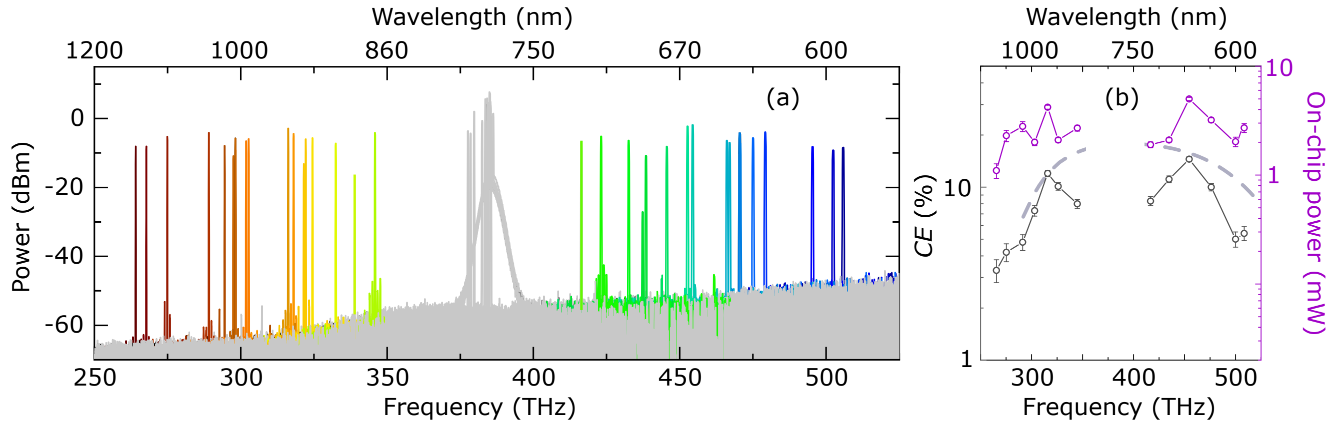

FIG. 3. **μOPO spectra, conversion efficiency, and output power.** (a) μOPO spectra from a series of devices recorded with an optical spectrum analyzer (OSA). No correction factors (e.g., from optical losses) are applied to these data. The transmitted pump light is shown in gray, and the signal/idler light is shown in color. (b) CE (gray) and P_i or P_s (purple; left and right portions of data, respectively) versus frequency, taking into account optical losses between the waveguide and OSA (see Supplemental Material). Error bars are estimated from the precision uncertainties in our measurements of optical power. The gray dashed line is a theoretical estimate of the maximum achievable CE based on our coupling measurements and Eq. 2.

nances. However, the relationship between κ and WW is more complex. Within the range of values considered, larger WW increases κ because the waveguide propagation constant shifts closer to the microring propagation constant, and the evanescent overlap between the microring and waveguide modes is not appreciably changed. At the same time, coupling resonances are redshifted. Figure 2b shows κ spectra for $G = 150$ nm, $L_\mathrm{p} = 3$ μm, and three values of WW. Apparently, the flattest κ spectra are realized for WW between 375 and 400 nm. After choosing WW, G may be chosen to realize critical coupling near ω_p.

To assess the accuracy of our simulations, we fabricate an array of SiN microrings with systematic coupling parameter variations (see Supplemental Material for details on our fabrication process), and we measure κ for each device. Specifically, we use either $L_\mathrm{p} = 0$ or $L_\mathrm{p} = 3$ μm, G between 110 nm and 160 nm, and WW between 350 nm and 400 nm. We carry out mode spectroscopy using a CW Titanium Sapphire (TiS) laser, which is tunable from 305 THz to 415 THz (720 nm to 980 nm), and from the microresonator transmission spectra we calculate K and κ values following Pfieffer *et al*[26]. In addition, we can perform sum frequency generation with the TiS laser and a 154 THz (1950 nm) laser to generate coherent light from 460 THz to 510 THz (590 nm to 650 nm). We find that simulations predict slightly larger κ values than we measure; to compensate, we reduce G by approximately 20 nm in experiments. In Fig. 2a, we present κ measurements (gray circles) of a straight-waveguide-coupled device with $WW = 375$ nm and $G = 125$ nm. The measured κ values are slightly lower than the corresponding simulation with $G = 150$ nm, but both data decrease exponentially with frequency, which is a known characteristic of straight-waveguide couplers[22]. Specifically, we measure $\kappa \approx 800$ MHz near 350 THz, but it drops sharply to $\kappa \approx 40$ MHz near 500 THz. In contrast, we observe a more achromatic κ spectrum in a pulley-waveguide-coupled device with $WW = 375$ nm, $G = 135$ nm, and $L_\mathrm{p} = 3$ μm. Our measurements (green circles) are shown in Fig. 2b, and they agree with the corresponding simulation with $G = 150$ nm. Our measurements indicate that, between 300 THz and 500 THz, κ takes on values over the relatively narrow range (compared to the straight-waveguide coupler) of 180 MHz to 400 MHz. We also measure $\gamma \approx 300$ MHz that is approximately independent of optical frequency for the wavelengths of interest (we have observed that γ increases at higher frequencies, but this behavior varies between different fabrication runs and requires further examination). Therefore, according to Eq. 2, our best pulley-waveguide-coupled devices should support many different μOPOs with $CE > 1\%$.

III. μOPO GENERATION AND CONVERSION EFFICIENCY MEASUREMENTS

To test our prediction, we record μOPO spectra with a calibrated optical spectrum analyzer (OSA) and calculate P_s, P_i, and CE values after accounting for optical losses between the waveguide and OSA (for details, see Supplemental Material). To generate μOPOs, we tune ω_p into resonance, starting blue detuned and decreasing ω_p until P_s and P_i are maximized. We repeat this procedure for different P_in values with the goal of maximizing CE. To ensure a variety of $\omega_{\mathrm{s(i)}}$ values, we engineer the GVD by systematically varying RW in different devices (see Ref.[15] and Supplemental Material). We utilize pulley-waveguide couplers such as those characterized in Fig. 2, and we find that CE is maximized for $L_\mathrm{p} = 3$ μm, WW between 375 nm and 400 nm, and G between 125 nm and 135 nm. In Fig. 3a, we present a compiled set of μOPO spectra that we extract from pulley-waveguide couplers with parameters in the above optimum range. In most cases, both P_s and P_i are greater than 1 mW, and P_in is typically between 30 mW and 45 mW. However, there are atypical μOPO spectra for which either P_s or P_i is $\ll 1$ mW. Most likely, these

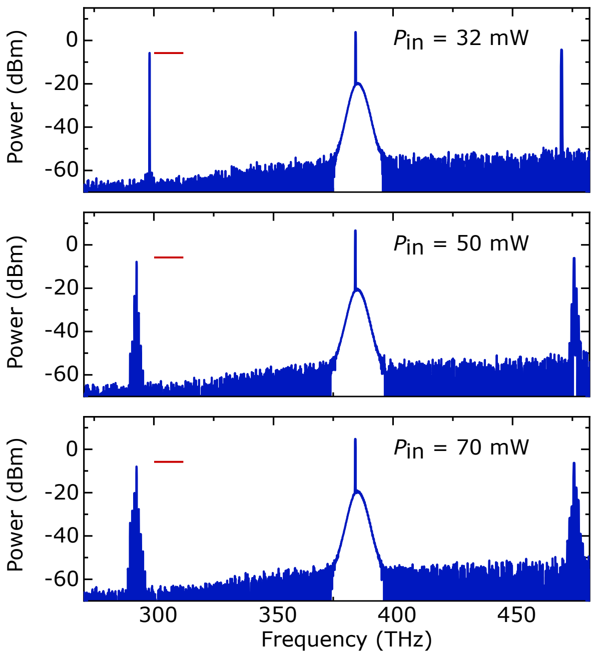

FIG. 4. **Mode competition constrains the μOPO output power.** The figure depicts μOPO spectra at three different pump powers, P_{in}. For $P_{\mathrm{in}} = 32$ mW (top panel), only the pump, signal, and idler modes oscillate. As P_{in} is increased (middle and bottom panels), mode switching occurs, and mode competitions distribute energy to modes other than the targeted signal/idler pair, leading to reduced $P_{\mathrm{s(i)}}$. To guide the eye, we include a red line in each panel that marks the top-panel P_{i} level.

result from mode interactions that locally alter the microring GVD and Q[27,28]. Table II in the Supplemental Material lists the individual pump, signal, and idler frequencies and powers for each μOPO spectrum shown in Fig. 3(a).

To characterize the μOPO performance, we calculate from Fig. 3a the largest values of P_{s} and P_{i} in spectral bins spanning approximately 20 THz each, and we plot the results in Fig. 3b along with the corresponding CE values. We find $P_{\mathrm{i}} > 1$ mW from 264 THz to 346 THz and $P_{\mathrm{i}} > 2$ mW from 275 THz to 346 THz. In the best case, we generate 4 mW of idler power at 315 THz using $P_{\mathrm{in}} = 34$ mW, which equates to $CE \approx 12\%$. Meanwhile, $P_{\mathrm{s}} > 1.9$ mW from 416 THz to 506 THz, and in the best case, we generate 5 mW of signal power at 454 THz using $P_{\mathrm{in}} = 34$ mW, which equates to $CE \approx 14.5\%$. Moreover, as expected from our simulations and measurements of κ and Eq. 2, CE decreases in the spectral wings as a result of smaller κ. Indeed, we can make a useful comparison between our CE measurements and a theoretical prediction (gray dashed line) based on our coupling measurements and Eq. 2. The central portion of data indicate CE values smaller than our theoretical prediction due to competing nonlinear processes that are exacerbated for narrow-band spectra[29]. Discrepancies at higher frequencies are primarily due to imperfect frequency mismatch arising from the stronger impact of higher-order dispersion. In between these extremes, we observe good agreement between our measurements and theory.

IV. LIMITATIONS ON OUTPUT POWER

Finally, we discuss the limits to μOPO output power and analyze an example. The relationship between $P_{\mathrm{s(i)}}$, P_{in}, and other experimental parameters has been analyzed theoretically[29]. Therein, it was predicted that $P_{\mathrm{s(i)}}$ increases with P_{in} for $P_{\mathrm{in}} \gtrsim P_{\mathrm{th}}$, but further increases in P_{in} lead to saturation or even reduction of $P_{\mathrm{s(i)}}$. The reason is that parasitic FWM processes compete with the targeted μOPO process. The predominant parasitic FWM process that we observe in experiments is mode competition between the targeted signal/idler modes and their spectral neighbors[29]. In Fig. 4, we show the μOPO spectrum for a single device as P_{in} is increased. For $P_{\mathrm{in}} = 32$ mW, only the pump, signal, and idler modes oscillate, and $P_{\mathrm{s(i)}} > 1$ mW (top panel). The idler power in this case is marked by the red line in each panel. When $P_{\mathrm{in}} = 50$ mW (middle panel), ω_{s} and ω_{i} shift to higher and lower frequencies, respectively. This behavior was predicted in Ref.[29] and termed ‘mode switching.’ In addition, other modes with frequencies close to $\omega_{\mathrm{s(i)}}$ begin to oscillate and steal energy from the μOPO. Hence, P_{i} decreases to a level below the red line, despite the increase in P_{in}. When P_{in} is further increased to 70 mW (bottom panel), $P_{\mathrm{s(i)}}$ remains approximately the same, but the power in the competing modes increases. The behavior demonstrated in this example is ubiquitous within our μOPO devices and explains why $P_{\mathrm{s(i)}}$ cannot be increased arbitrarily by increasing P_{in}. Still, increasing CE and $P_{\mathrm{s(i)}}$ beyond the levels we demonstrate may be possible using alternate phase- and frequency-matching strategies, such as that reported in Ref.[30]. As it stands, the achieved power levels are relevant for some applications, such as spectroscopy of various coherent near-infrared and visible systems[31,32].

V. DISCUSSION

In conclusion, we have demonstrated energy-efficient μOPOs with practically-relevant output powers in a crucial portion of the visible and near-infrared spectrum. Our results are enabled by broadband pulley-waveguide couplers that we design using coupled-mode simulations. For the most widely-separated μOPOs, we observe relatively lower CE values that are consistent with undercoupled signal and idler modes. Hence, an important focus for future work is to extend the spectral bandwidth over which devices are nearly critically coupled, thus broadening the range of frequencies that can be efficiently extracted into a single waveguide. Other possible approaches include using frequency-specific coupling geometries (e.g., one may optimize κ at the μOPO-specific frequencies ω_{s} and ω_{p}, while neglecting the idler), or to couple multiple waveguides - each designed for different portions of the μOPO spectrum - to one microring. Moreover, new strategies should be devised to avoid parasitic FWM processes and increase the realizable output power. Nonetheless, our work is a compelling demonstration that μOPOs can help satisfy the demand for compact sources of visible laser light.

VI. SUPPLEMENTARY MATERIAL

The supplemental material describes how the microresonator geometry is controlled to engineer GVD for μOPO, explains our conversion efficiency calculations, and details our device fabrication.

ACKNOWLEDGMENTS

We thank Khoi Hoang and Tahmid Sami Rahman for carefully reading the manuscript and giving useful feedback. This project is funded by the DARPA LUMOS and NIST-on-a-chip programs.

DATA AVAILABILITY STATEMENT

The data that support the findings of this study are available from the corresponding author upon reasonable request.

[1] T. Bothwell, C. J. Kennedy, A. Aeppli, D. Kedar, J. M. Robinson, E. Oelker, A. Staron, and J. Ye, "Resolving the gravitational redshift across a millimetre-scale atomic sample," Nature **602**, 420–424 (2022).

[2] D. Awschalom, K. K. Berggren, H. Bernien, S. Bhave, L. D. Carr, P. Davids, S. E. Economou, D. Englund, A. Faraon, M. Fejer, *et al.*, "Development of quantum interconnects (quics) for next-generation information technologies," PRX Quantum **2**, 017002 (2021).

[3] L. E. M. Matheus, A. B. Vieira, L. F. Vieira, M. A. Vieira, and O. Gnawali, "Visible light communication: concepts, applications and challenges," IEEE Communications Surveys & Tutorials **21**, 3204–3237 (2019).

[4] R. Weissleder, "A clearer vision for in vivo imaging," Nature Biotechnology **19**, 316–317 (2001).

[5] J. N. Tinsley, S. Bandarupally, J.-P. Penttinen, S. Manzoor, S. Ranta, L. Salvi, M. Guina, and N. Poli, "Watt-level blue light for precision spectroscopy, laser cooling and trapping of strontium and cadmium atoms," Optics Express **29**, 25462–25476 (2021).

[6] D. C. Parrotta, A. J. Kemp, M. D. Dawson, and J. E. Hastie, "Multiwatt, continuous-wave, tunable diamond raman laser with intracavity frequency-doubling to the visible region," IEEE Journal of Selected Topics in Quantum Electronics **19**, 1400108–1400108 (2013).

[7] R. P. Mildren, H. M. Pask, H. Ogilvy, and J. A. Piper, "Discretely tunable, all-solid-state laser in the green, yellow, and red," Optics Letters **30**, 1500–1502 (2005).

[8] K. J. Vahala, "Optical microcavities," Nature **424**, 839–846 (2003).

[9] T. Kippenberg, S. Spillane, and K. Vahala, "Kerr-nonlinearity optical parametric oscillation in an ultrahigh-q toroid microcavity," Physical Review Letters **93**, 083904 (2004).

[10] N. L. B. Sayson, T. Bi, V. Ng, H. Pham, L. S. Trainor, H. G. Schwefel, S. Coen, M. Erkintalo, and S. G. Murdoch, "Octave-spanning tunable parametric oscillation in crystalline kerr microresonators," Nature Photonics **13**, 701–706 (2019).

[11] C. S. Werner, T. Beckmann, K. Buse, and I. Breunig, "Blue-pumped whispering gallery optical parametric oscillator," Optics Letters **37**, 4224–4226 (2012).

[12] Y. Jia, K. Hanka, K. T. Zawilski, P. G. Schunemann, K. Buse, and I. Breunig, "Continuous-wave whispering-gallery optical parametric oscillator based on cdsip2," Optics Express **26**, 10833–10841 (2018).

[13] X. Lu, G. Moille, A. Singh, Q. Li, D. A. Westly, A. Rao, S.-P. Yu, T. C. Briles, S. B. Papp, and K. Srinivasan, "Milliwatt-threshold visible–telecom optical parametric oscillation using silicon nanophotonics," Optica **6**, 1535–1541 (2019).

[14] J. Lu, A. Al Sayem, Z. Gong, J. B. Surya, C.-L. Zou, and H. X. Tang, "Ultralow-threshold thin-film lithium niobate optical parametric oscillator," Optica **8**, 539–544 (2021).

[15] X. Lu, G. Moille, A. Rao, D. A. Westly, and K. Srinivasan, "On-chip optical parametric oscillation into the visible: generating red, orange, yellow, and green from a near-infrared pump," Optica **7**, 1417–1425 (2020).

[16] D. J. Moss, R. Morandotti, A. L. Gaeta, and M. Lipson, "New CMOS-compatible platforms based on silicon nitride and Hydex for nonlinear optics," Nature Photonics **7**, 597–607 (2013).

[17] H. Park, C. Zhang, M. A. Tran, and T. Komljenovic, "Heterogeneous silicon nitride photonics," Optica **7**, 336 (2020).

[18] S. Fujii, S. Tanaka, M. Fuchida, H. Amano, Y. Hayama, R. Suzuki, Y. Kakinuma, and T. Tanabe, "Octave-wide phase-matched four-wave mixing in dispersion-engineered crystalline microresonators," Optics Letters **44**, 3146–3149 (2019).

[19] Y. Tang, Z. Gong, X. Liu, and H. X. Tang, "Widely separated optical Kerr parametric oscillation in AlN microrings," Optics Letters **45**, 1124–1127 (2020).

[20] R. R. Domeneguetti, Y. Zhao, X. Ji, M. Martinelli, M. Lipson, A. L. Gaeta, and P. Nussenzveig, "Parametric sideband generation in cmos-compatible oscillators from visible to telecom wavelengths," Optica **8**, 316–322 (2021).

[21] R. W. Boyd, *Nonlinear optics* (Academic press, 2020).

[22] G. Moille, Q. Li, T. C. Briles, S.-P. Yu, T. Drake, X. Lu, A. Rao, D. Westly, S. B. Papp, and K. Srinivasan, "Broadband resonator-waveguide coupling for efficient extraction of octave-spanning microcombs," Optics Letters **44**, 4737–4740 (2019).

[23] E. Shah Hosseini, S. Yegnanarayanan, A. H. Atabaki, M. Soltani, and A. Adibi, "Systematic design and fabrication of high-Q single-mode pulley-coupled planar silicon nitride microdisk resonators at visible wavelengths," Optics Express **18**, 2127 (2010).

[24] Q. Li, M. Davanço, and K. Srinivasan, "Efficient and low-noise single-photon-level frequency conversion interfaces using silicon nanophotonics," Nature Photonics **10**, 406–414 (2016).

[25] W.-P. Huang, "Coupled-mode theory for optical waveguides: an overview," Journal of the Optical Society of America A **11**, 963–983 (1994).

[26] M. H. Pfeiffer, J. Liu, M. Geiselmann, and T. J. Kippenberg, "Coupling ideality of integrated planar high-q microresonators," Physical Review Applied **7**, 024026 (2017).

[27] T. Herr, V. Brasch, J. Jost, I. Mirgorodskiy, G. Lihachev, M. Gorodetsky, and T. Kippenberg, "Mode spectrum and temporal soliton formation in optical microresonators," Physical Review Letters **113**, 123901 (2014).

[28] S. Ramelow, A. Farsi, S. Clemmen, J. S. Levy, A. R. Johnson, Y. Okawachi, M. R. Lamont, M. Lipson, and A. L. Gaeta, "Strong polarization mode coupling in microresonators," Optics Letters **39**, 5134–5137 (2014).

[29] J. R. Stone, G. Moille, X. Lu, and K. Srinivasan, "Conversion efficiency in kerr-microresonator optical parametric oscillators: From three modes to many modes," Physical Review Applied **17**, 024038 (2022).

[30] F. Zhou, X. Lu, A. Rao, J. Stone, G. Moille, E. Perez, D. Westly, and K. Srinivasan, "Hybrid-mode-family kerr optical parametric oscillation for robust coherent light generation on chip," Laser & Photonics Reviews , 2100582 (2022).

[31] X. Xu, B. Sun, P. R. Berman, D. G. Steel, A. S. Bracker, D. Gammon, and L. J. Sham, "Coherent optical spectroscopy of a strongly driven quantum dot," Science **317**, 929–932 (2007).

[32] D. V. Brazhnikov, S. M. Ignatovich, I. S. Mesenzova, A. M. Mikhailov, R. Boudot, and M. N. Skvortsov, "Two-frequency sub-doppler spectroscopy of the caesium D1 line in various configurations of counterpropagating laser beams," Quantum Electronics **50**, 1015 (2020).